Bulletin of the Seismological Society of America, Vol. 99, No. 3, pp. 1953–1961, June 2009, doi: 10.1785/0120080168

P- and *S*-Wave Receiver Function Images of Crustal Imbrication beneath the Cheyenne Belt in Southeast Wyoming

by Steven Hansen and Ken Dueker

Abstract We extend the receiver function deconvolution methodology of Bostock (2004) to *S*-wave receiver functions and develop a method of source function spectrum estimation to constrain the crustal structure across the Archean–Proterozoic Cheyenne belt suture in southeast Wyoming using data from a dense deployment of seismic stations. *S*-wave receiver functions are particularly useful because free-surface reverberations do not contaminated the direct $S_d p$ arrivals, and the *S*-wave receiver function image is able to validate our *P*-wave receiver function image. *P*- and *S*-wave receiver function images and a teleseismic *P*-wave tomogram find a structure consistent with the imbrication of Proterozoic lower crust across the Cheyenne belt. Both *P* and *S*-wave receiver function images delineate a double Moho north of the Cheyenne belt: the Archean Moho is imaged at 41–43 km depth with a deeper velocity step at 60–62 km depth. South of the Cheyenne belt, the *P*-wave receiver function image finds the Proterozoic Moho dipping ~7° northwest consistent with observed back-azimuth dependent $P_m s$ amplitudes. Given the lateral continuity with the northwest dipping Proterozoic Moho, the deeper velocity step of the double Moho is interpreted as the imbricated Proterozoic Moho. Modeling of *P*-wave receiver function amplitudes suggests a 6.4–7.4 km/sec velocity step across the shallower Archean Moho and a 7.4–7.9 km/sec velocity step across the deeper imbricated Proterozoic Moho. We speculate that imbrication of the Proterozoic lower crust was contemporaneous with the 1.76 Ga uplift and deformation of the 50 km-wide Palmer Canyon block immediately north of the Cheyenne belt exposed in the Laramie Mountains.

Introduction

The Cheyenne belt is a fundamental lithospheric boundary between the Wyoming Archean craton and the >1000 km of accreted Paleoproterozoic crust to the south (Sims and Stein, 2003). Accretion at the southern margin of the Wyoming craton initiated with the 1.78–1.75 Ga Medicine Bow orogeny (Chamberlain, 1998; Tyson *et al.*, 2002). During the Medicine Bow orogeny, the Proterozoic Green Mountain arc collided with the passive margin of the Wyoming craton via south facing (outboard directed) subduction (Tyson *et al.*, 2002). The Laramie Peak shear zone is an ~10 km thick mylonitic shear zone that formed contemporaneously with the Cheyenne belt and demarcates the Laramie Peak block to the north from the Palmer Canyon block to the south (Fig. 1) (Chamberlain *et al.*, 1993; Resor and Snoke, 2005). Thermobarometric estimates of metamorphic *P–T* conditions suggest that the Palmer Canyon block was uplifted 10–15 km with respect to the Laramie Peak block at 1.76 Ga (Chamberlain *et al.*, 1993; Patel *et al.*, 1999). The Palmer Canyon block uplift is hypothesized to have formed as a result of thrust faulting along with significant internal block deformation; however, the exact fault kinematics, that is, planar or listric, and the relationship between the uplift of the Palmer Canyon block and the formation of the Cheyenne belt is largely unconstrained (Resor and Snoke, 2005).

To date, several refraction studies in southern Wyoming and northern Colorado have found that crustal thickness increases across the Cheyenne belt from 40–46 km beneath the southern Wyoming Archean craton to 45–54 km beneath the Proterozoic Colorado province (Prodehl and Lipman, 1989; Snelson *et al.*, 1998; Levander *et al.*, 2005; Snelson *et al.*, 2005). These refraction findings are in good agreement with teleseismic receiver function studies from the Lodore array, which traversed the Cheyenne belt 200 km west of our study area. These results find a 50–63 km thick crust directly south of the of the Cheyenne belt (Crosswhite and Humphreys, 2003; Poppeliers and Pavlis, 2003). Thus, it appears that the crustal architecture established during the formation of the Cheyenne belt has remained to present times.

It is important to note that seismic reflection results from the Sierra Madre (Morozova *et al.*, 2005), and the Laramie

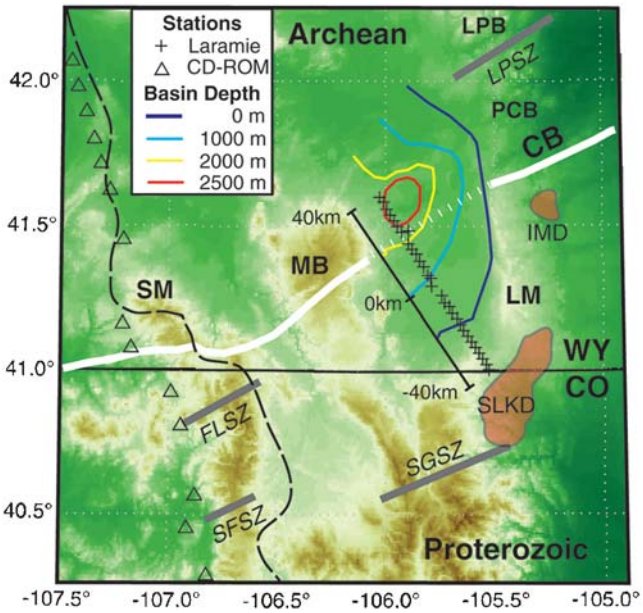

Figure 1. Topography, stations, and crustal shear zones. Geographic features denoted as: Sierra Madres, SM; Medicine Bow Mountains, MB; Laramie Mountains, LM. In the Laramie Mountains, the Palmer Canyon block (PCB) and Laramie Peak block (LPB) are labeled. The black dashed line denotes the CDROM refraction line and the nearby triangles are the broadband seismometers. The Cheyenne belt suture (CB) is the white line, dashed where inferred. Other major shear zones are denoted with gray lines: Laramie Peak shear zone, LPSZ; Farwell Mountain–Lester Mountain suture zone, FLSZ; Soda Creek-Fish Creek shear zone, SFSZ; Skin Gulch shear zone, SGSZ. The location of the Stateline Kimberlite District (SLKD) and Iron Mountain District (IMD) are shaded red.

Mountains (Allmendinger *et al.*, 1982; Speece *et al.*, 1994) lack distinct Moho reflections directly south of the Cheyenne belt. In addition, a wide angle seismic experiment was unable to image a distinct Moho reflection beneath the Laramie Mountains (Gohl and Smithson, 1994). A nonreflective Proterozoic Moho could occur for several reasons: a gradational velocity boundary, a highly scattering boundary, or a small impedance contrast (Gohl and Smithson, 1994; Morozova *et al.*, 2005). The lack of a well-defined reflection Moho across the Cheyenne belt in southeast Wyoming provides motivation for this study.

To better constrain the structure of the Cheyenne belt, a dense 60 km long line array of broadband seismometers was deployed within the Laramie basin, which traversed the inferred trace of the Cheyenne belt (Fig. 1). The Laramie array consisted of 30 sensors spaced 2.2 km apart and was deployed for a period of eight months in 2000–2001. In this study, *P*- and *S*-wave receiver functions are processed to produce common conversion point (CCP) images of converted wave amplitudes. In addition, a teleseismic *P*-wave tomography model is presented.

Both *P*- and *S*-wave receiver function datasets have unique strengths and weaknesses that must be considered when comparing the two CCP images. The *S*-wave receiver function image (henceforth *S*-wave image) is not contaminated by free-surface reverberations because, with respect to the direct *S*-wave arrival, S_dp waves arrive precursory whereas free-surface reverberations arrive postcursory (Wilson *et al.*, 2006; Yuan *et al.*, 2006). The lack of free-surface reverberations within the time window containing S_dp arrivals makes *S*-wave receiver functions an invaluable aid for identifying free-surface reverberations that contaminate a *P*-wave receiver function image (henceforth *P*-wave image). For example, the northern end of the Laramie array is underlain by 2–3 km of sediments (Fig. 1), and free-surface reverberations reflected from the basement-sediment contact obscure direct P_ds arrivals from the midcrust. On the other hand, there are two factors that degrade the *S*-wave image with respect to the *P*-wave image. First, the *S*-wave receiver function dataset has lower data folds due to the limited range of epicentral distances for *S* and *SKS* arrivals that are not contaminated by secondary arrivals (Wilson *et al.*, 2006; Yuan *et al.*, 2006). Second, *S*-wave receiver functions have lower frequency content (3–6 sec period) with respect to *P*-wave receiver functions (1–2 sec period) resulting in a lower resolution image. This difference in frequency content between *P*- and *S*-wave receiver functions is due to the larger path attenuation of teleseismic *S* waves with respect to *P* waves.

Data

Our *P*-wave receiver function dataset is constructed from 58 *P*-wave events at 30°–100° epicentral distance with body-wave magnitudes > 5.6, and our *S*-wave receiver function dataset is constructed from five *S*-wave and four *SKS* events from 55°–85° and > 85° epicentral distances, respectively (Fig. 2). For *S* wave and *SKS* arrivals, the distance range is restricted to avoid interference with secondary arrivals (Wilson *et al.*, 2006; Yuan *et al.*, 2006). *S*-wave events are visually inspected and only events with *SV*-dominant polarization and low pre-event noise are used. All events are rotated into the *P*–*SV*–*SH* coordinate system (Vinnik, 1977) and band-pass-filtered at 0.1–1 Hz and 0.05–0.5 Hz for the *P*- and *S*-wave receiver function datasets. For our

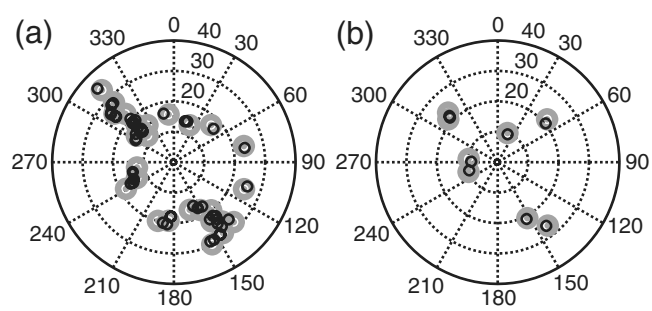

Figure 2. Polar plots of teleseismic events and event bins used in receiver function processing. Black circles denote events and gray circles denote event bins. (a) *P*-wave events. (b) *S*-wave events. The radial distance is the estimated angle of incidence of the direct arrival at the surface.

P-wave tomography model, 1600 travel-time residuals are measured from 78 teleseismic *P*-wave events using a multichannel cross-correlation algorithm (VanDecar and Crosson, 1990). The arrival times are inverted for *P*-wave velocity perturbation using a standard least-squares algorithm resulting in a 74% variance reduction of the *P*-wave residuals (Newton, 2004).

Receiver Function Methodology

The events recorded by each station are binned by back-azimuth and ray parameter producing 26 *P*- and 8 *S*-wave event bins (Fig. 2). The events are binned in slowness space using square nonoverlapping bins with a width of 0.01 sec/km. The mean number of events per bin is 2.2 and 1.1 for *P*- and *S*-wave events, respectively. One three-component receiver function is estimated per bin per station resulting in a total of 627 *P*- and 207 *S*-wave receiver functions for the array.

Our deconvolution scheme is based upon a new methodology that explicitly includes pure-mode scattering that arrives on the direct arrival component, that is, *P*–*P* scattering on the *P*-component *P*-wave receiver function and *S*–*S* scattering on the *SV*-component *S*-wave receiver function. This technique exploits the quasi minimum-phase nature of the direct component receiver function and results in a full three-component receiver function estimate for each event bin (Bostock, 2004; Baig *et al.*, 2005; Mercier *et al.*, 2006).

A three-component seismic trace is modeled as a convolution:

$$\mathbf{x}(t) = s(t) * \mathbf{g}(t), \tag{1}$$

where bold type variables are vectors, $\mathbf{x}(t)$ is the three-component seismic trace, $s(t)$ is the source function, $\mathbf{g}(t)$ is the three-component receiver function, and $*$ denotes convolution. In the log-spectral domain, the convolution in equation (1) becomes additive:

$$\log\{|\mathbf{X}(\omega)|\} = \log\{|S(\omega)|\} + \log\{|\mathbf{G}(\omega)|\}, \tag{2}$$

where $|\mathbf{X}(\omega)|$ is the amplitude spectra of the three-component seismic trace, $|S(\omega)|$ is the spectrum of the source function, and $|\mathbf{G}(\omega)|$ is the receiver function spectra. In equation (2), the amplitude spectra are used instead of the complex spectra to avoid the phase unwrapping problem associated with computing the log spectrum (Ulrych, 1971).

Using equation (2), the M events recorded in each event bin are represented by a system of $3M$ spectral equations. This system of equations is inherently subrank by one equation: having $M + 3$ unknowns and a rank of $M + 2$ (Bostock, 2004). To resolve this rank deficiency, the system of equations is augmented by M initial estimates of the source function spectra (discussed subsequently) resulting in an over determined system:

$$\begin{bmatrix} \mathbf{I}_3 & \mathbf{1} & \cdots & 0 \\ 0 & \mathbf{1} & \cdots & 0 \\ \vdots & \vdots & \ddots & \vdots \\ \mathbf{I}_3 & 0 & \cdots & \mathbf{1} \\ 0 & 0 & \cdots & \mathbf{1} \end{bmatrix} \begin{bmatrix} \log\{|\mathbf{G}(\omega)|\} \\ \log\{|S_1(\omega)|\} \\ \vdots \\ \log\{|S_M(\omega)|\} \end{bmatrix} = \begin{bmatrix} \log\{|\mathbf{X}_1(\omega)|\} \\ \log\{|\tilde{S}_1(\omega)|\} \\ \vdots \\ \log\{|\mathbf{X}_M(\omega)|\} \\ \log\{|\tilde{S}_M(\omega)|\} \end{bmatrix}, \tag{3}$$

where $\mathbf{I}_3$ is the 3 by 3 identity matrix, $\mathbf{1} = [1, 1, 1]^T$, and $|\tilde{S}_M(\omega)|$ is the Mth source function spectrum estimate (Baig *et al.*, 2005; Mercier *et al.*, 2006). The model vector is estimated via a least-squares inversion of equation (3) at each frequency and contains log-spectral amplitude estimates of the three-component receiver function and the updated source functions.

The phase spectra are reconstructed by applying all-pass filters to the estimated receiver function amplitude spectra. Suitable all-pass filters can be estimated if one component of the receiver function is minimum phase (Bostock, 2004). For *P*-wave receiver functions, Bostock (2004) showed that the *P*-component receiver function is effectively minimum phase due to the fact that this component is dominated by the direct *P*-wave arrival that is followed by low amplitude scattered waves. In the case of *S*-wave receiver functions, the *SV*-component receiver function contains scattered arrivals at both positive and negative lag times with respect to the direct *S*-wave arrival resulting in a mixed phase spectrum. In practice, however, the seismic trace is windowed to include the direct arrival and the 50 sec prior to the direct arrival, then reversed in time for receiver function processing. This results in an *SV*-component trace whose amplitude is dominated by the direct arrival followed by the low amplitude scattered waves making the trace near minimum phase. Hence, it is possible to extend the phase reconstruction methodology of Bostock (2004) to *S*-wave receiver functions.

The initial source function spectra used in equation (3) are estimated from the observed seismic traces by exploiting differences in the spectral roughness between the source function and the propagational Green's function (i.e., receiver function). The source function is assumed to have a smooth and bandlimited spectrum, similar to the theoretical ω-squared source function model (Aki, 1967); although, the source function spectrum is notably roughened by source side scattering (e.g., Warren and Shearer, 2005) and slip-heterogeneities during fault dislocation (Hisada, 2001), which creates spectral holes. In contrast, the receiver function is a sparse spike train in the time domain that can be modeled as a Cauchy distribution (Escalante *et al.*, 2007) having a rough, oscillating amplitude spectrum that is quasi-white. In the log-spectral domain, the spectrum of the observed seismic trace results from the addition of the smooth source function and rough receiver function log spectra (equation 2). Thus, an initial source spectrum estimate can be calculated by simply smoothing the observed log spectrum. A similar approach has been used for wavelet

estimation in active source seismic studies (Rosa and Ulrych, 1991; Claerbout, 1992; Tavares *et al.*, 2005).

The log spectrum of a recorded *P*- or *SV*-component seismic trace is smoothed by fitting a piecewise continuous cubic spline function to the observed spectrum. Smoothness is enforced by penalizing the second derivative of the spline function. The optimal smoothing spline is determined by minimizing the cost function:

$$p\sum_{i=1}^{n}[\log\{|X(\omega_i)|\} - f(\omega_i)]^2 + (1-p)\int f''(\omega)^2\,d\omega, \quad (4)$$

where $f(\omega)$ is the spline function and p controls the trade-off between data fit and smoothness of the spline (De Boor, 2001). For source estimation, a value of 10^{-5} for $(1-p)$ is used and yields a good fit to the spectrum; using $(1-p)$ values ranging from 10^{-4} to 10^{-6} produces similar results. To produce a single source function spectrum estimate per event, the smoothed spectra for all 30 stations are linearly stacked. Figure 3 shows an example of a source function spectrum estimate and the resulting receiver function spectra for a single *P*-wave event. Although it is difficult to determine exactly how smooth the source function spectrum should be, this method of smoothing captures the broad structure of the source spectra, including a small spectral oscillation at 0.6–0.8 Hz, resulting in a relatively white receiver function spectrum.

P- and *S*-wave receiver functions are mapped to depth via the CCP stacking technique (Dueker and Sheehan, 1998) using a *P*-wave velocity model adapted from the Continental Dynamics of the Rocky Mountains (CDROM) refraction model across the Cheyenne belt (Levander *et al.*, 2005). An *S*-wave velocity model is estimated assuming an average crustal V_P/V_S ratio of 1.77 (Christensen and Mooney, 1995). The CCP bin size is 1 km vertically by 15 km and 20 km horizontally for the *P*- and *S*-wave images, respectively.

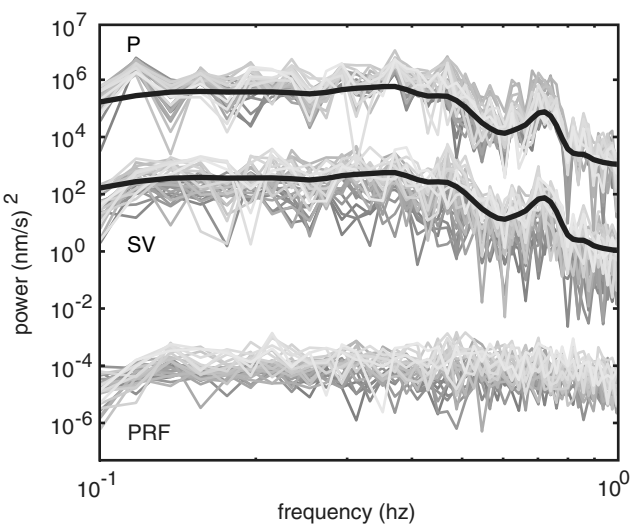

Figure 3. Source function estimation for a *P*-wave event. The power spectra of the recorded seismic traces and the resulting receiver functions are labeled and plotted as gray lines. The *P*- and *SV*-component spectra are offset for clarity and labeled. The black lines denote the estimated power spectrum of the source function as a result of stacking the spline smoothed *P*-component spectra. The *P*-wave receiver function spectra are the result the least-squares inversions of equation (3).

Results

The basement-sediment contact beneath the Laramie basin is identified in the *P*-wave image (Fig. 4a) as the positive high amplitude arrival in the uppermost crust that dips to the northwest. This arrival deepens to ~4 km depth north of the Cheyenne belt where the Laramie basin is thickest (Fig. 1). The basement-sediment contact is also identified in the *S*-wave image (Fig. 4b) as the shallow high amplitude arrival that deepens to the northwest; although, this basin arrival is poorly resolved due to the lower frequency content of the *S*-wave data. Interpretation of the *P*-wave image requires care due to the influence of free-surface reverberations back scattered at the basement-sediment contact. These reverberations are imaged as a set of three alternating high amplitude peaks at 12–22 km depth north of the Cheyenne belt. The negative arrival at 12 km depth is most likely the phase PpP_bp, where except for the first letter, uppercase letters denote down going legs of the multiple, lowercase letters denote up going legs, and the subscript b denotes back scattering at the basement-sediment contact. The PpP_bp phase is followed by the positive amplitude PpP_bs at 20 km depth and the negative amplitude PpS_bs at 22 km depth. The interpretation of these *P*-wave receiver function arrivals as basin reverberations is consistent with the *S*-wave image, which finds no structure in this interval because the *S*-wave receiver functions are not contaminated by free-surface multiples (Wilson *et al.*, 2006; Yuan *et al.*, 2006).

Beneath the southeast half of the array, the *P*-wave image finds a positive amplitude arrival at 50–55 km depth dipping to the northwest that we interpret as the Proterozoic Moho. This result is consistent with previous seismic results that find the crust thickening northward to 50–60 km just south of the Cheyenne belt (Crosswhite and Humphreys, 2003; Poppeliers and Pavlis, 2003; Gilbert and Sheehan, 2004; Levander *et al.*, 2005). The *S*-wave image finds the Moho at a similar depth range, but the dip is poorly constrained. The difference in Moho dip between the *P*- and *S*-wave images is attributable to several factors: the lower folds of the *S*-wave data, the increased divergence of the S_dp rays at Moho depths with respect to P_ds rays (Fig. 5), and the influence of out of plane *S*-wave events.

North of the Cheyenne belt, both the *P*- and *S*-wave images reveal a positive amplitude arrival at 41–43 km depth that terminates laterally beneath the downward projection of the Cheyenne belt; this arrival is interpreted as the Archean Moho. We are confident that this arrival is not a basin reverberation for three reasons: (1) the P_ds-arrival time is too late to be a free-surface reverberation from the basement-sediment

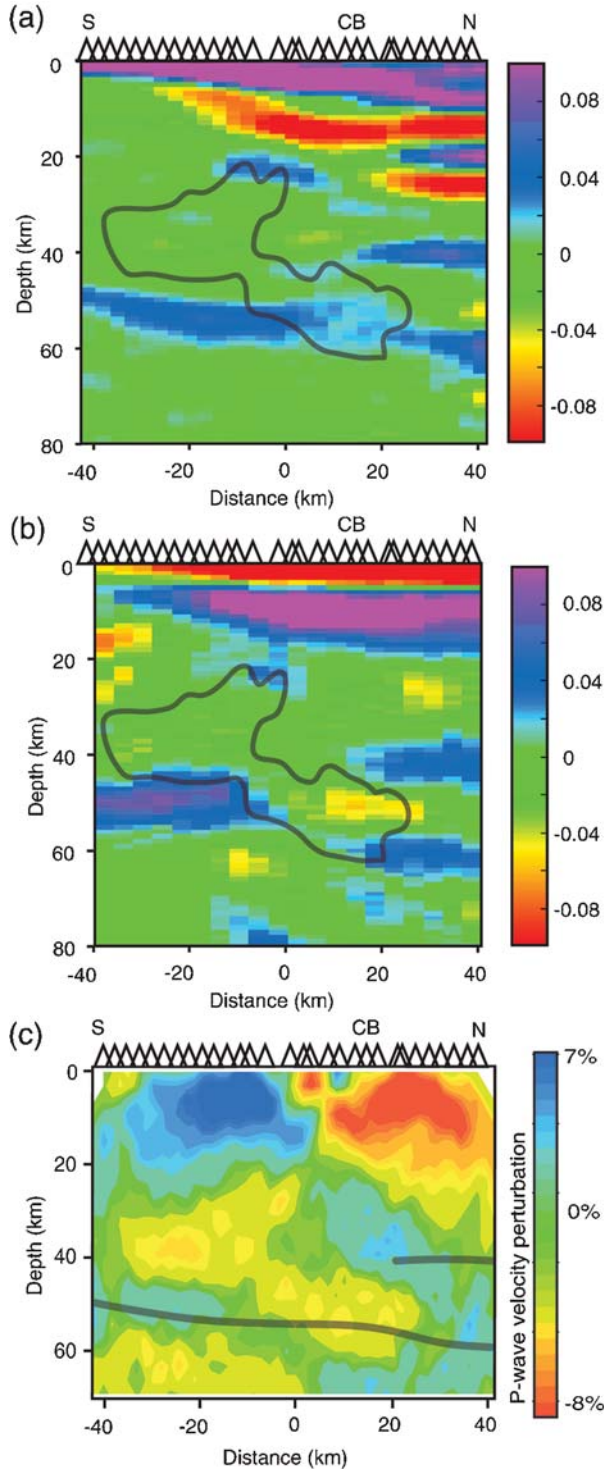

Figure 4. Laramie array results. Triangle symbols denote the station locations and the Cheyenne belt (CB) is labeled. (a) *P*-wave receiver function image. (b) *S*-wave receiver function image. (c) Teleseismic *P*-wave tomography model. The gray lines denoted the base of the Archean and Proterozoic crust interpreted from (a). In (b) the image is muted from 60 to 80 km depth between −20 and −40 km distance due to a lack of data in this region, for example, see Figure 5b. Blue and red colors in (a) and (b) denote positive and negative shear velocity contrasts with respect to increasing depth. The gray line on images (a) and (b) is the −3.5% *P*-wave velocity perturbation contour from (c).

contact; (2) the *S*-wave image, which is unaffected by free-surface multiples, agrees well with the *P*-wave image; and (3) an ~40 km Moho depth is consistent with previous estimates of Archean crustal thickness from active source studies north of the Cheyenne belt in southern Wyoming (Allmendinger *et al.*, 1982; Prodehl and Lipman, 1989; Snelson *et al.*, 1998; Morozova *et al.*, 2002).

Below the Archean Moho, both the *P*- and *S*-wave images find a second positive amplitude arrival at 60–62 km depth. In the *P*-wave image, this arrival is laterally contiguous with the northwest dipping Proterozoic Moho found beneath the southern stations; hence, this arrival is interpreted as imbricated Proterozoic crust. Thus, the two arrivals together create a double-Moho structure north of the Cheyenne belt. In the *S*-wave image, this deep arrival is not laterally continuous with respect to the Proterozoic Moho south of the Cheyenne belt where the ray sampling is poorest and out of plane events dominate the sampling (Fig. 5b). Thus, the discrepancy between these two images is likely due to differences in data folds and ray kinematics. A double-Moho structure is consistent with the receiver function image from the Lodore array, which finds positive amplitude arrivals at 35 and 55 km depth just north of the Cheyenne belt (Poppeliers and Pavlis, 2003).

The most prominent feature of the *P*-wave tomography model (Fig. 4c) is the 14% lateral *P*-wave velocity contrast in the upper 15 km of crust. This velocity contrast can be explained by the thickening of Laramie basin sediments to the northwest (Fig. 1) and by the ~0.5 km/sec velocity contrast in the upper crust across the Cheyenne belt found by the refraction study of Gohl and Smithson (1994). In the Proterozoic lower crust, a low velocity body (i.e., the −3.5% contour) is found that dips to the north and extends to a depth of 61 km beneath the Cheyenne belt. This low velocity body likely manifests the lateral velocity contrast between the lower crust across the Cheyenne belt. Refraction results from the CDROM experiment find that the Proterozoic crust is 0.1–0.4 km/sec slower than the crust north of the Cheyenne belt below 30 km depth (Levander *et al.*, 2005).

The *P*-wave image finds an ~7° northward dip of the Proterozoic Moho that deepens from 50 km at the southern end of the array to 60 km at the northern end. A dipping velocity interface will produce significant $P_d s$ amplitude modulation with respect to back azimuth and provides a test to confirm the imaged dip (Cassidy, 1992). As shown in Figure 4a, the amplitude of the $P_m s$ arrival at the ten southeastern stations varies by ~50% between northwest and southeast back-azimuth *P*-wave receiver function gathers (Fig. 6a). The observed amplitudes are modeled using Zoeppritz equations (Aki and Richards, 2002) to estimate the velocity of the lower crust. Assuming an upper-mantle *P*-wave velocity of 7.95 km/sec below the Cheyenne belt (Levander *et al.*, 2005) and a 7° northwest dipping Moho, the observed amplitude modulation requires a 6.66 ± 0.15 km/sec lower crust *P*-wave speed. This result is consistent with *P*-wave velocity measurements of lower crustal

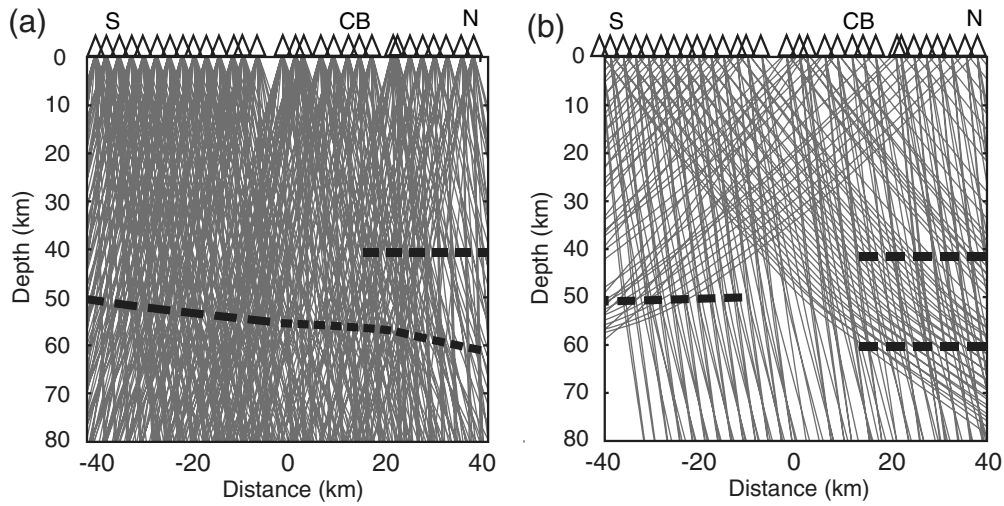

Figure 5. Converted wave ray paths. (a) $P_d s$ rays for P-wave receiver functions. (b) $S_d p$ rays for S-wave receiver functions. The dashed lines show the locations of the Archean and Proterozoic Moho as interpreted from the CCP images (Fig. 4b,c). The rays in (a) that appear to be near normal incidence are the projection of out of plane events (Fig. 2b).

xenoliths from the Stateline Kimberlite District (Farmer *et al.*, 2005) (Fig. 1) and the velocity models from the CDROM and deep probe refraction experiments (Snelson *et al.*, 1998; Levander *et al.*, 2005; Snelson *et al.*, 2005), which find velocities of 6.5–7.1 km/sec in the Proterozoic lower crust.

The mean P- and S-wave receiver function stacks from the six northernmost stations find the double-Moho arrivals at 41–43 km and 60–62 km depth (Fig. 6b) and can be used to constrain the velocity of the imbricated layer. The crustal layering beneath these six stations is relatively flat; and hence one-dimensional amplitude modeling can be applied. The stacked P-wave receiver function amplitudes are modeled using a simple two layer velocity model (Fig. 6c). Remarkably, modeling of the S-wave receiver function amplitudes results in a velocity model that differs by <0.1 km/sec from the model shown in Figure 6c although the range of velocity models that fit the data is increased due to the larger error of these measurements. While there are important differences in the methodology and dataset between this study and the velocity models from the CDROM refraction experiment (Levander *et al.*, 2005; Snelson *et al.*, 2005), it is useful to compare these results. Above the Archean Moho, our best-fit velocity model finds a 6.4 km/sec Archean lower crust, which is consistent with the velocities measured from the Leucite Hills xenoliths (Farmer *et al.*, 2005) and the CDROM refraction models (Fig. 6b). Below the Archean Moho our model finds that the imbricated layer is 7.4 km/sec. Although a velocity of 7.4 km/sec is not unreasonable for arc lower crust (Holbrook *et al.*, 1999), neither the CDROM nor the deep probe refraction results found such high velocity lower crust beneath the Cheyenne belt. These refraction experiments were conducted >100 km to the west of this study area; and thus structural heterogeneity may account for these differences. Conversely, the refraction study of Gohl and Smithson (1994) in the central Laramie Mountains found a 6.5–7.5 km/sec lower crust.

Conclusions

We have processed P- and S-wave receiver function datasets by extending the methodology of Bostock (2004) to S-wave data by noting the minimum-phase nature of the SV-component receiver function that is windowed and time reversed. This methodology requires an initial estimate of the source function amplitude spectrum, which is estimated via spline smoothing the log spectra of the observed seismic data. This approach exploits the inherent spectral differences between the relatively smooth source function and the rough receiver function.

CCP stacking of P- and S-wave receiver functions has yielded two independent images of the subsurface beneath the Laramie array. Although there are important caveats when comparing the P- and S-wave images, the two images (Fig. 4a,b) are consistent with an imbricated Moho north of the Cheyenne belt. The S-wave image, albeit of lower frequency and fold, provides first-order constraints for the robust identification of direct $P_d s$ arrivals in the P-wave image, which can be obscured by interfering free-surface multiples produced by the Laramie basin.

The most remarkable result from this study is the double Moho imaged beneath the Archean crust in both the P- and S-wave images. This structure is manifest by positive amplitude arrivals at 42 and 61 km depth. We interpret this observation to be indicative of crustal imbrication whereby the Proterozoic lower crust was underthrust beneath the Archean crust (Fig. 7). Three lines of evidence support this interpretation. First, the Proterozoic Moho is imaged as dipping ~7° to the northwest south of the Cheyenne belt in the P-wave image. A dipping Moho is supported by the observed back-azimuth dependant $P_m s$ amplitudes (Fig. 6a) and the northwest dipping structure observed in the P-wave tomography model (Fig. 4c). Second, the dipping Proterozoic Moho is laterally contiguous with the deep arrival north

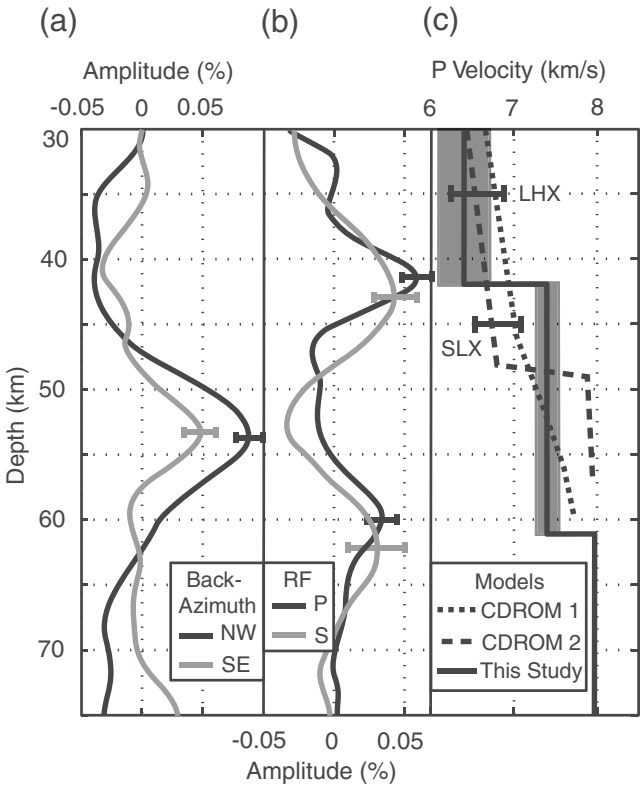

Figure 6. Seismic amplitude modeling. (a) *P*-wave receiver function stacks from northwest (NW) and southeast (SE) back-azimuth gathers for the ten southernmost stations for 0.04–0.06 sec/km ray parameter events. (b) *P*- and *S*-wave receiver function stacked trace with bootstrapped standard errors from the six northernmost stations. (c) *P*-wave velocity models that explain the observed amplitudes from (b). The black line denotes the best-fit model, and the gray shading represents velocity models fitting the observed amplitudes within one standard error. The dashed lines show the CDROM refraction models from Snelson *et al.* (2005) (denoted CDROM 1) and Levander *et al.* (2005) (denoted CDROM 2). The black horizontal bars show the measured xenolith velocities from Leucite Hills (LHX) and the State Line diatremes (SLX) (Farmer *et al.*, 2005).

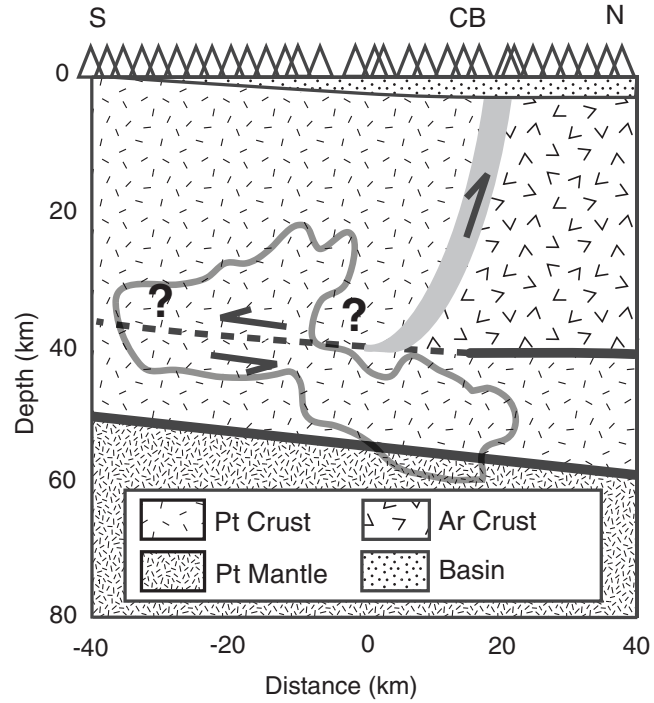

Figure 7. Geologic interpretation. The location of the Cheyenne belt (gray line) is inferred from the lateral termination of the Archean Moho observed in Figure 3. The underthrusting of the Proterozoic lower crust is accommodated by the mid-crustal shear zone, denoted by the dashed black line. The sense of shearing on the Cheyenne belt and the mid-crustal shear zone are denoted by arrows. The Archean Moho and Proterozoic Moho from the *P*-wave receiver function image (Fig. 4a) are denoted by thick black lines. The gray line on the images is the −3.5% *P*-wave velocity perturbation contour from Figure 4c.

of the Cheyenne belt below the Archean Moho. Third, *P*-wave receiver function amplitude modeling suggests that the rock between the Archean and Proterozoic Moho has a velocity of 7.4 km/sec, which is too low to be a mantle velocity. Because of the limited aperture of the Laramie array, the northern extent of Proterozoic underthrusting is unknown; and hence these results only provide a minimum estimate of ~20 km of crustal imbrication. To directly test our imbrication hypothesis, more seismic data are needed to determine the northern extent of the double-Moho structure.

The imbrication of Proterozoic crust beneath the Cheyenne belt in southeast Wyoming is consistent with the interpretation of the seismic results from the CDROM project (Tyson *et al.*, 2002; Yuan and Dueker, 2005; Zurek and Dueker, 2005). In addition, our *P*-wave image is strikingly similar to that of Poppeliers and Pavlis (2003) from the Lodore array that crossed the Cheyenne belt in northwest Colorado. The general agreement of several seismic results along the strike of the Cheyenne belt suggests that lower crustal imbrication is perhaps ubiquitous along the Cheyenne belt.

An important question that remains is the timing of imbrication beneath the Cheyenne belt. In the Laramie Mountains, the 1.76 Ga uplift and deformation of the Palmer Canyon block (Fig. 1) is the last recorded compressional deformation event north of the Cheyenne belt (other than the 60 Ma east–west directed Laramide uplift); and thus a plausible hypothesis is that crustal imbrication was coeval with the uplift of the Palmer Canyon block during the Medicine Bow orogeny. If this hypothesis is correct, then our observations are consistent with a growing body of research that suggests crustal imbrication is a pervasive process during accretion along cratonic margins (e.g., Snyder, 2002; Moore and Wiltschko, 2004).

Data and Resources

The seismograms used in this study were collected from the Laramie telemetered broadband array using Program for Array Seismic Studies of the Continental Lithosphere

(PASSCAL) instruments. The data are available from the Incorporated Research Institutions for Seismology (IRIS) data management center at www.iris.edu (last accessed March 2009).

Acknowledgments

We thank the IRIS PASSCAL instrument center for use of the telemetered broadband seismic array.

References

Aki, K. (1967). Scaling law of seismic spectrum, *J. Geophys. Res.* **72,** no. 4, 1217–1231.

Aki, K., and P. G. Richards (2002). *Quantitative Seismology*, Second Ed., University Science Books, Sausilito, California, ISBN 0-935702-96-2, 704 pp.

Allmendinger, R. W., J. A. Brewer, L. D. Brown, S. Kaufman, J. E. Oliver, and R. S. Houston (1982). COCORP profiling across the Rocky Mountain Front in southern Wyoming; Part 2, Precambrian basement structure and its influence on Laramide deformation, *GSA Bull.* **93,** 1253–1263.

Baig, A. M., M. Bostock, and J. P. Mercier (2005). Spectral reconstruction of teleseismic *P* Green's functions, *J. Geophys. Res.* **110,** B08306, doi 10.1029/2005JB003625.

Bostock, M. (2004). Green's functions, source signatures, and the normalization of teleseismic wave fields, *J. Geophys. Res.* **109,** B03303, doi 10.1029/2003JB002783.

Cassidy, J. F. (1992). Numerical experiments in broadband receiver function analysis, *Bull. Seismol. Soc. Am.* **82,** 1453–1474.

Chamberlain, K. (1998). Medicine Bow orogeny: Timing of deformation and model of crustal structure produced during continent-arc collision, ca. 1.78 Ga, southeastern Wyoming, *Rocky Mt. Geol.* **33,** 259–277.

Chamberlain, K. R., S. C. Patel, B. R. Frost, and G. L. Snyder (1993). Thick-skinned deformation of the Archean Wyoming Province during Proterozoic arc-continent collision (with Suppl. Data 9339), *Geology* **21,** 995–998.

Christensen, N. I., and W. D. Mooney (1995). Seismic velocity structure and composition of the continental crust: A global view, *J. Geophys. Res.* **100,** no. B6, 9761–9788.

Claerbout, J. F. (1992). *Earth Soundings Analysis: Processing Versus Inversion*, Blackwell Scientific, Boston.

Crosswhite, J. A., and E. D. Humphreys (2003). Imaging the mountainless root of the 1.8 Ga Cheyenne belt suture and clues to its tectonic stability, *Geology* **31,** 669–672, doi 10.1130/G19552.1.

De Boor, C. (2001). *A Practical Guide to Splines*, Springer, New York.

Dueker, K. G., and A. F. Sheehan (1998). Mantle discontinuity structure beneath the Colorado Rocky Mountains and High Plains, *J. Geophys. Res.* **103,** no. B4, 7153–7169.

Escalante, C., Y. J. Gu, and M. Sacchi (2007). Simultaneous iterative time-domain sparse deconvolution to teleseismic receiver functions, *Geophys. J. Int.* **171,** 316–325.

Farmer, G. L., S. A. Bowring, M. L. Williams, N. I. Christensen, J. P. Matzel, and L. Stevens (2005). Contrasting lower crustal evolution across an Archean–Proterozoic suture: Physical, chemical, and geochronologic studies of lower crustal xenoliths in southern Wyoming and northern Colorado, in *The Rocky Mountain Region—An Evolving Lithosphere: Tectonics, Geochemistry, and Geophysics*, K. E. Karlstrom and G. R. Keller (Editors), American Geophysical Union, Washington, D.C., 139–162.

Gilbert, H. J., and A. F. Sheehan (2004). Images of crustal variations in the intermountain west, *J. Geophys. Res.* **109,** B03306, doi 10.1029/2003JB002730.

Gohl, K., and S. B. Smithson (1994). Seismic wide-angle study of accreted Proterozoic crust in southeastern Wyoming, *Earth Planet. Sci. Lett.* **125,** 293–305.

Hisada, Y. (2001). A theoretical omega-square model considering spatial variation in slip and rupture velocity. Part 2: Case for a two-dimensional source model, *Bull. Seismol. Soc. Am.* **91,** 651–666.

Holbrook, W. S., D. Lizarralde, S. McGeary, N. Bangs, and J. Diebold (1999). Structure and composition of the Aleutian island arc and implications for continental crustal growth, *Geology* **27,** 31–34.

Levander, A., C. Zelt, and M. B. Magnani (2005). Crust and upper mantle velocity structure of the southern Rocky Mountains from the Jemez Lineament to the Cheyenne belt, in *The Rocky Mountain Region—An Evolving Lithosphere: Tectonics, Geochemistry, and Geophysics*, K. E. Karlstrom and G. R. Keller (Editors), American Geophysical Union, Washington, D.C., 293–308.

Mercier, J. P., M. Bostock, and A. M. Baig (2006). Improved Green's functions for passive source structural studies, *Geophysics* **22,** SI95–SI102, doi 10.1190/1.2213951.

Moore, V. M., and D. V. Wiltschko (2004). Syncollisional delamination and tectonic wedge development in convergent orogens, *Tectonics* **23,** TC2005, doi 10.1029/2002TC001430.

Morozova, E., I. B. Morozov, N. K. Boyd, R. A. Johnson, K. E. Karlstrom, A. R. Tyson, C. T. Foster, X. Wan, K. R. Chamberlain, and S. B. Smithson (2002). Geometry of Proterozoic sutures in the central Rocky Mountains from seismic reflection data: Cheyenne belt and Farwell Mountain structures, *Geophys. Res. Lett.* **29,** no. 13, 1639, doi 10.1029/2001GL013819.

Morozova, E. A., X. Wan, K. R. Chamberlain, S. B. Smithson, R. Johnson, and K. E. Karlstrom (2005). Inter-wedging nature of the Cheyenne belt–Archean–Proterozoic suture defined by seismic reflection data, in *The Rocky Mountain Region—An Evolving Lithosphere: Tectonics, Geochemistry, and Geophysics*, K. E. Karlstrom and G. R. Keller (Editors), American Geophysical Union, Washington, D.C., 217–226.

Newton, S. A. (2004). Lithospheric velocity structure beneath the Laramie array of southeastern Wyoming, *Master's Thesis*, University of Wyoming, Laramie, Wyoming.

Patel, S. C., B. R. Frost, K. R. Chamberlain, and G. L. Snyder (1999). Proterozoic metamorphism and uplift history of the north–central Laramie Mountains, Wyoming, USA, *J. Metamorph. Geol.* **17,** 243–258.

Poppeliers, C., and G. L. Pavlis (2003). Three-dimensional, prestack, plane wave migration of teleseismic *P*-to-*S* converted phases: 2. Stacking multiple events, *J. Geophys. Res.* **108,** no. B5, 2267, doi 10.1029/2001JB001583.

Prodehl, C., and P. W. Lipman (1989). Crustal structure of the Rocky Mountain region, in *Geophysical Framework of the Continental United States*, C. P. Louis and D. M. Walter (Editors), Geological Society of America (GSA), Boulder, Colorado, 249–284.

Resor, P. G., and A. W. Snoke (2005). Laramie Peak shear system, central Laramie Mountains, Wyoming, USA: Regeneration of the Archean Wyoming province during Palaeoproterozoic accretion, *Geol. Soc. London, Spec. Publ.* **245,** 81–107, doi 10.1144/GSL.SP.2005.245.01.05.

Rosa, A. L., and T. J. Ulrych (1991). Processing via spectral modeling, *Geophysics* **56,** 1244–1251.

Sims, P. K., and H. J. Stein (2003). Tectonic evolution of the Proterozoic Colorado province, southern Rocky Mountains: a summary and appraisal, *Rocky Mt. Geol.* **38,** 183–204.

Snelson, C. M., T. J. Henstock, G. R. Keller, K. C. Miller, and A. Levander (1998). Crustal and uppermost mantle structure along the deep probe seismic profile, *Rocky Mt. Geol.* **33,** 181–198.

Snelson, C. M., G. R. Keller, K. C. Miller, H.-M. Rumpel, and C. Prodehl (2005). Regional crustal structure derived from the CD-ROM 99 seismic refraction/wide-angle reflection profile: the lower crust and upper mantle, in *The Rocky Mountain Region—An Evolving Lithosphere: Tectonics, Geochemistry, and Geophysics*, K. E. Karlstrom and G. R. Keller (Editors), American Geophysical Union, Washington, D.C., 271–291.

Snyder, D. B. (2002). Lithospheric growth at margins of cratons, *Tectonophysics* **355,** 7–22.

Speece, M. A., B. R. Frost, and S. B. Smithson (1994). Precambrian basement structure and Laramide deformation revealed by seismic reflection profiling in the Laramie Mountains, Wyoming, *Tectonics* **13,** 354–366.

Tavares, D. M., L. S. Lucena, H. A. Schots, E. C. Mundim, and F. J. Herrmann (2005). The deconvolution of seismic data as a fluctuation analysis, *Integr. Comput.-Aided Eng.* **12,** 25–42.

Tyson, A. R., S. B. Smithson, K. G. Dueker, C. T. Foster, E. A. Morozova, K. E. Karlstrom, and K. R. Chamberlain (2002). Proterozoic Farwell Mountain–Lester Mountain suture zone, northern Colorado: Subduction flip and progressive assembly of arcs, *Geology* **30,** 943–946.

Ulrych, T. J. (1971). Application of homomorphic deconvolution to seismology, *Geophysics* **36,** 650–660.

VanDecar, J. C., and R. S. Crosson (1990). Determination of teleseismic relative phase velocity arrival times using multi-channel cross-correlation and least squares, *Bull. Seismol. Soc. Am.* **80,** 150–169.

Vinnik, L. P. (1977). Detection of waves converted from *P* to *SV* in the mantle, *Phys. Earth Planet. Interiors* **15,** 39–45.

Warren, L. M., and P. M. Shearer (2005). Using the effects of depth phases on *P*-wave spectra to determine earthquake depths, *Bull. Seismol. Soc. Am.* **95,** 173–184.

Wilson, D. C., D. A. Angus, J. F. Ni, and S. P. Grand (2006). Constraints on the interpretation of *S*-to-*P* receiver functions, *Geophys. J. Int.* **165,** 969–980, doi 10.1111/j.1365-246X.2006.02981.x.

Yuan, H., and K. Dueker (2005). Upper mantle tomographic V_P and V_S images of the Rocky Mountains in Wyoming, Colorado, and New Mexico: Evidence for thick, laterally heterogeneous lithosphere, in *The Rocky Mountain Region—An Evolving Lithosphere: Tectonics, Geochemistry, and Geophysics*, K. E. Karlstrom and G. R. Keller (Editors), American Geophysical Union, Washington, D.C., 329–345.

Yuan, X., R. Kind, X. Li, and R. Wang (2006). The *S* receiver functions: Synthetics and data example, *Geophys. J. Int.* **165,** 555–564, doi 10.1111/j.1365-246X.2006.02885.x.

Zurek, B., and K. Dueker (2005). Lithospheric stratigraphy beneath the southern Rocky Mountains, in *The Rocky Mountain Region—An Evolving Lithosphere: Tectonics, Geochemistry, and Geophysics*, K. E. Karlstrom and G. R. Keller (Editors), American Geophysical Union, Washington, D.C., 317–328.

University of Wyoming
Department of Geology and Geophysics
Department 3006
1000 University Avenue
Laramie, Wyoming 82071

Manuscript received 3 July 2008